Nano Research

Open Access

Research Article

Sound frequency sensitive triboelectric nanogenerator for multi-functional auditory perceptual system applications

Si Yuan Zhou, Wei Sheng Wang, Xin Huang, Bei Chen Gong, Jia Kang Di, You Jie Huang, and Li Qiang Zhu ✉

School of Physical Science and Technology, Ningbo University, Ningbo 315211, China

Cite this article: *Nano Research*, **2025**, *18*, 94907378. https://doi.org/10.26599/NR.2025.94907378

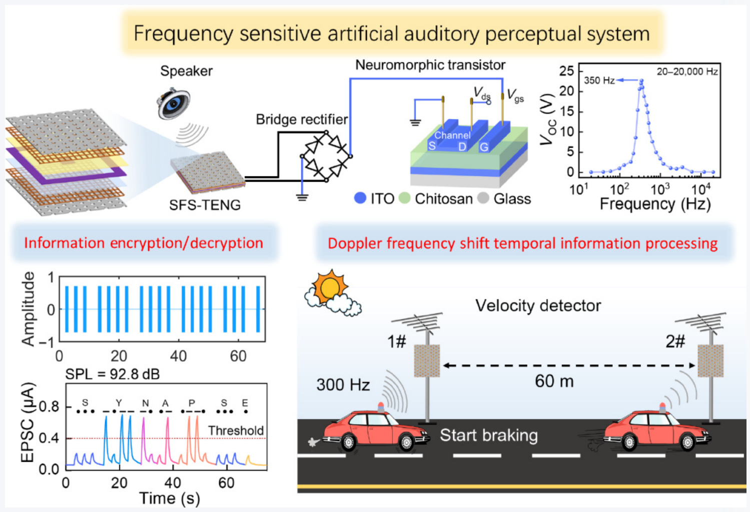

ABSTRACT: Hardware based neuromorphic sensory system has attracted great attention for cognitive interactive platform. Auditory perception system can capture and analyze various sound signals, helping us to detect dangerous surroundings and judge environmental conditions. Therefore, developing neuromorphic auditory system that can decode auditory spatiotemporal information would be interesting. Here, an artificial auditory perceptual system is proposed by integrating sound frequency sensitive triboelectric nanogenerators (SFS-TENGs) and oxide based ionotronic neuromorphic transistor. With perforated configuration, the SFS-TENG adopting polyetheretherketone membrane and polytetrafluoroethylene membrane as friction layers can convert sound wave signals into electrical signals, exhibiting a high sensitivity of ~ 2.24 V/dB and good durability. The neuromorphic transistor can further process electrical signals generated by SFS-TENG. Thus, the system can mimic auditory perception, exhibiting a wide range of sound pressure and frequency recognition capabilities. Information encryption/decryption and Doppler frequency shift temporal information processing are demonstrated on the TENG based auditory system for the first time. The present auditory perceptual system demonstrates broad application prospects, providing new opportunities to create sophisticated, adaptable, and interactive systems.

KEYWORDS: ionotronic neuromorphic transistor, artificial auditory perceptual system, Doppler frequency shift, sound encryption and decryption function

1 Introduction

With the deep learning technology, artificial intelligence (AI) is developing rapidly, permeating almost every aspect of our daily life with the fields of image, voice, and natural language [1]. However, current AI technology predominantly relies on von Neumann architecture based on big data and complex programming codes in a sequential computation mode. Such architecture separates computation unit and storage unit physically, greatly limiting the computing efficiency [2–4]. Inspired by the energy efficient parallel computing scheme through hierarchical neural networks of the brain, neuromorphic computing has been proposed to overcome the dilemma of the AI technology [5–7]. As an important branche in neuromorphic engineering, neuromorphic devices have also been proposed as the fundamental building blocks for AI, including two-terminal memristor based ones [8–11] and three terminal transistor based ones [12–15], demonstrating rich synaptic functions and neuromorphic functions. Additionally, human perceptual system possesses the capabilities of hybrid multi-modal sensory activities, endowing us the capability of deep interacting with our surroundings. Thus, hardware based neuromorphic sensory system has attracted great attention for human–machine interface [16–18], artificial intelligence [19–21], and biomimetic perception [22–24]. Especially, biomimetic perceptual systems can simulate various perceptual functions,

Received: December 25, 2024; **Revised:** February 26, 2025
Accepted: March 17, 2025

✉Address correspondence to zhuliqiang@nbu.edu.cn

including tactile perception [25–27], visual recognition [28, 29], multi-modal perception [30], etc.

As one of the most efficient perceptual systems for human being, auditory perception helps us to obtain over 10% information in daily activities. Figure 1(a) schematically shows the auditory perceptual system. Sound causes the eardrum to vibrate, and the hair cells in the cochlea convert these mechanical vibrations into action potentials, which are integrated through synapses and transmitted to the brain through the auditory nerve. After processing these signals, the auditory perception is formed. Such perceptual mechanisms can help human being to perceive sounds in environment, respond to danger signals, and ensure their own safety [31, 32]. Inspired by the auditory perceptual mechanism, artificial auditory perceptual systems were proposed [33–35]. It should be noted here that wireless sense is needed in such perceptual systems. Due to the limited energy supply of these systems, the requirements for low energy consumption becomes prominent for long-term service. Interestingly, triboelectric nanogenerators (TENGs) can sensitively convert environmental energy into electrical signals, demonstrating great self-powered ability [36–39]. Moreover, TENGs are flexible and versatile in material and structural selection. By designing specific structures, TENGs can perceive various sound signals [40, 41]. It should be noted here that complex software units are still required to analyze the characteristics of these signals. Therefore, integrating TENGs with neuromorphic devices can achieve real-time computation of sound signals and rich neuromorphic functions [42–45]. However, researchers usually use sound signals of fixed frequencies to modulate the transistor performances, which greatly limits the functions of the system [46, 47]. Interestingly, frequency of sound would affect the output voltage of TENGs. Additionally, Doppler effect will be triggered when there is a relative velocity between the sound source and the observer, i.e., the sound frequency will change [48, 49]. Thus, the investigation of artificial auditory perceptual system under the stimuli of sound with different frequencies would be interesting and extend application prospects.

In this work, an artificial auditory perceptual system is proposed by integrating sound frequency sensitive triboelectric nanogenerators (SFS-TENGs) with indium tin oxide (ITO) based ionotronic neuromorphic transistors. As schematically shown in Fig. 1(b), the SFS-TENG can convert sound wave signals into electrical signals, which are loaded to the in-plane gate of the transistor, triggering neuromorphic information processing. The SFS-TENG exhibits a high sensitivity of ~ 2.24 V/dB and good durability. It has a wide range of sound pressure and frequency recognition capabilities. Thus, information encryption/decryption function and Doppler frequency shift temporal information processing are demonstrated on the SFS-TENG based auditory perceptual system for the first time. The present auditory perceptual system demonstrates broad application prospects, providing new opportunities to create sophisticated, adaptable, and interactive systems.

2 Experimental

2.1 Fabrication of SFS-TENG

Figure 1(c) schematically shows the structure of SFS-TENG. It is composed of perforated acrylic sheets, copper meshes, polyetheretherketone (PEEK) membrane, polytetrafluoroethylene (PTFE) membrane, and rectangular annular paper strip. To obtain the upper electrode, a copper mesh was attached to a perforated acrylic sheet. Then, a PEEK membrane with thickness of ~ 0.4 mm was attached to the copper mesh to act as friction layer. To obtain the lower electrode, another copper mesh was attached to another perforated acrylic sheet. A PTFE membrane with thickness of ~ 0.5 mm was attached to the copper mesh. Next, a rectangular annular paper strips with thickness of ~ 0.1 mm was placed around and in the center of the PTFE membrane to act as a spacer, as shown in Fig. 1(d). Finally, the upper electrode and lower electrode were assembled and fixed with a tape to obtain the SFS-TENG. The length and the width of the SFS-TENG were 4 cm. The thickness of the SFS-TENG was ~ 2.2 mm. Figure 1(e) shows the scanning electron microscopy (SEM) image of the copper mesh. The length of square aperture was ~ 0.18 mm. The diameter of the copper wire was ~ 0.07 mm. As shown in Fig. 1(f), the aperture and spacing of perforated acrylic sheets are both ~ 1 mm, much larger than the aperture of copper mesh. Two sets of wires can be drawn out from the copper mesh of the upper and lower electrodes for testing. In our previous works, there were no holes on the upper electrodes

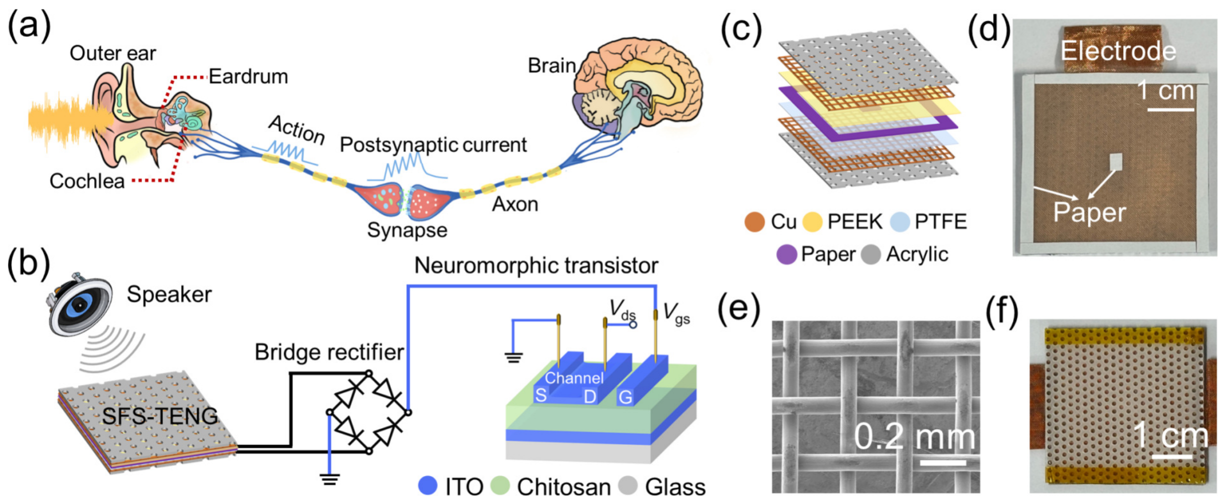

Figure 1 (a) Schematic diagram of the human auditory perceptual system. (b) Schematic diagram of the proposed artificial auditory perceptual system integrated with SFS-TENG and ITO neuromorphic transistor. (c) Schematic diagram of SFS-TENG. (d) Photograph of paper strip on the PTFE membrane. (e) SEM image of copper mesh. (f) Photograph of perforated acrylic sheet.

and lower electrodes [50]. Thus, sounds were difficult to pass through the two electrodes and trigger obvious triboelectric response on the previous reported TENG. To solve this limitation, perforated acrylic sheets were introduced. The holes on the acrylic sheets would let sound pass through easily, reducing the reflection and loss of sound waves. The structure help effective mechanical interaction between PTFE and PEEK to trigger obvious triboelectric response. The copper mesh can adapt well to the vibration and deformation generated by sound waves, ensuring the stable performances of the SFS-TENG.

2.2 Fabrication of ITO neuromorphic transistor

Figure S1(a) in the Electronic Supplementary Material (ESM) schematically shows the device processing of the ITO neuromorphic transistor. Firstly, chitosan solution was obtained by dissolving 2 wt.% chitosan powder and 2 wt.% acetic acid in 96 wt.% deionized water. Then, the solution was drop-coated on ITO glass substrates, followed by drying at 50 °C for 7 h to form a chitosan-based solid state electrolyte film. The chitosan solution was also drop-coated on a silicon substrate. After drying, the chitosan film can be peeled off from the substrate. Then, the film was cooled in liquid nitrogen and gently pressed with tweezers to obtain film fragments. Subsequently, ITO electrodes and channels were deposited on the chitosan film by sputtering ITO target (In_2O_3:SnO_2 = 90:10 wt.%) using a metal shadow mask under pure Ar ambient. During sputtering, DC power, sputtering pressure, and Ar flow rate were set to 80 W, 0.8 Pa, and 42 sccm, respectively. Due to the reflection of ITO nanoparticles at the mask edge, a thin ITO channel layer can be formed between source (S) and drain (D) electrodes. Interestingly, in-plane gate (G) can also be formed. The inset in Fig. S1(a) in the ESM shows the photograph of the in-plane-gate ITO neuromorphic transistor.

2.3 Characterization and electrical measurements

Thicknesses of chitosan film were characterized using SEM. Surface morphologies of the PEEK membrane, the PTFE membrane, and the chitosan film were characterized using atomic force microscopy (AFM). Frequency dependent specific capacitance of chitosan based electrolyte film was characterized by using an IM3533 impedance analyzer. Figure S1(b) in the ESM shows physical image of testing figuration for SFS-TENG. A speaker (HPS01) was adopted to load sound on SFS-TENG. Output voltage (V_{OC}) of SFS-TENG was measured with an oscilloscope (MSO22). Figure S1(c) in the ESM shows physical image of testing figuration for neuromorphic transistor. Inset is enlarged physical image of the neuromorphic transistor. Electrical performances of the oxide neuromorphic transistor were measured with a semiconductor parameter analyzer (Keithley 4200A SCS). All the electrical characterizations were performed in a dark shielded box with air relative humidity of ~ 50%.

3 Results and discussion

Figure 2(a) shows cross-sectional SEM image of the chitosan film. The thickness is ~ 30.1 μm. There are no pinholes within the films, as is helpful for good electrical performances. Figure 2(b) shows AFM surface morphology image of the chitosan film. The surface Rms value is ~ 1.42 nm. Figure 2(c) shows frequency dependent capacitance of the chitosan based electrolyte film. A big specific capacitance of ~ 1.6 μF/cm^2 is obtained at 1 Hz. It is related to the formation of electric-double-layer (EDL) at the chitosan/ITO interface. Figure 2(d) shows output curves measured at V_{gs} ranged from −0.3 to 2.4 V with steps of 0.3 V. The results indicate good ohmic contact at the S/D electrode. Figure 2(e) shows five repeated transfer curves of the ITO neuromorphic transistor. Anti-clockwise hysteresis window of ~ 0.4 V is observed. The behaviors can be attributed to the migration of protons within the chitosan-based electrolyte. These curves approach each other very well, indicating good stabilities. The leakage current is also quite small (< 10 nA), as shown in Fig. S2(a) in the ESM. The ON/OFF ratio, subthreshold swing, threshold voltage, and mobility are estimated to be ~ 3.4 × 10^5, ~ 171 mV/dec, ~ 0.1 V, and ~ 0.8 cm^2/(V·s), respectively.

In nervous system, excitatory post-synaptic current (EPSC) will be triggered when excitatory neurotransmitters bind to receptors on post-synapse. It plays a crucial role in neural signal transmission. Owing to the proton related EDL effects, EPSC responses could be mimicked on the ITO neuromorphic transistor. The EPSC response can be detected with a constant V_{ds} of 0.5 V. Figure 2(f) shows EPSC responses triggered by spikes with different durations. The EPSC peak value increases from ~ 3.3 to ~ 10.9 μA with the increased spike duration from 10 to 40 ms. Meanwhile, spike amplitude also affects the EPSC response, as shown in Fig. S2(b) in the ESM. The EPSC peak value increases from ~ 0.8 to ~ 6.3 μA with the increased spike amplitude from 1 to 4 V. Additionally, spikes with different shapes would also induce different EPSC responses. The left panel of Fig. 2(g) shows EPSC response triggered by a step-like spike with gradually increased amplitudes from 0.5 to 4 V with steps of 0.5 V within 80 ms. The EPSC increases gradually until the spike ends. The peak EPSC value is ~ 8.4 μA. The right panel of Fig. 2(g) shows EPSC response triggered by a step-like spike with gradually decreased amplitudes from 4 to 0.5 V with steps of 0.5 V within 80 ms. The peak EPSC value is only ~ 6.9 μA. Interestingly, the peak value is arrived at the time when the spike does not end. When the initial potential is large, protons within the chitosan electrolyte will quickly accumulate at the chitosan/ITO interface. While the followed lower potential has no enough driving force to accumulate more protons at the interface. Thus, accumulated protons tend to return to equilibrium position, though there are followed weak potential. On the contrary, protons will receive increased driven force when receiving spike with gradually increased potentials. Thus, protons will gradually accumulate at the chitosan/ITO interface until the spike ends. Figure 2(h) shows typical EPSC response triggered by paired gate spikes (4 V, 10 ms) with an interval time (ΔT) of 10 ms. The second EPSC peak value (A_2) is higher than the first one (A_1). Thus, biological paired-pulse facilitation (PPF) effects have been mimicked. Here, PPF index is defined as $(A_2 - A_0)/(A_1 - A_0) \times 100\%$, where A_0 is the initial resting current. Thus, PPF index is ~ 141.8% when ΔT is 10 ms. Figure 2(i) shows PPF index as a function of ΔT. The curve can be fitted by a double exponential decay function

$$\text{PPF index} = 1 + C_1 \cdot \exp(-\Delta T/\tau_1) + C_2 \cdot \exp(-\Delta T/\tau_2) \quad (1)$$

where C_1 (C_2) and τ_1 (τ_2) are initial facilitation magnitudes and characteristic relaxation times of the two decay phases, respectively. The fitting gives C_1, C_2, τ_1, and τ_2 values of ~ 28.2%, ~ 20.7%, ~ 33.3 ms, and ~ 536.7 ms, respectively. When ΔT is small, the PPF index drops sharply with the increased ΔT value. When ΔT is high, the PPF index drops gently until it approaches ~ 100%.

The working mechanism of TENG can be generally described as

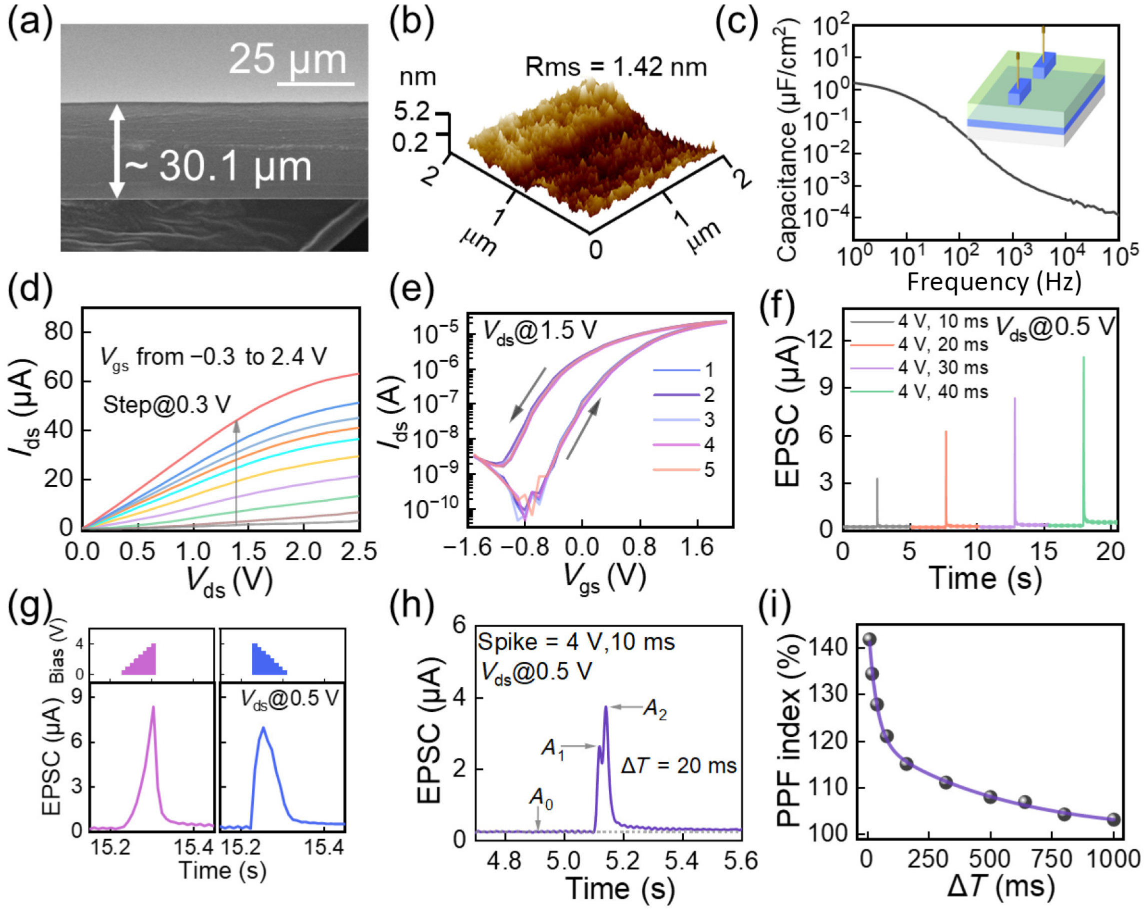

Figure 2 (a) Cross-sectional SEM image of the chitosan film fragments. (b) AFM surface morphology of the chitosan film coated on glass substrate. (c) Frequency dependent capacitance of the chitosan-based electrolyte film. Inset: In-plane gated test structure. (d) Output curves of the ITO neuromorphic transistor. (e) Five repeated transfer curves of the ITO neuromorphic transistor. (f) Typical EPSC responses triggered by spikes with different duration times. (g) EPSC responses triggered by step-like spike with gradually increased amplitudes and gradually decreased amplitudes. (h) Typical EPSC response triggered by paired gate spikes (4 V, 10 ms) with ΔT of 20 ms. (i) PPF index as a function of ΔT value.

follows [36, 37]. When two different friction layers contact with each other under external force, opposite charges will be carried on their surfaces. Thus, a potential difference will be triggered if the two friction layers separate, resulting in the generation of current in external circuit. Thus, TENG can collect energy from mechanical vibration, which can be used for self-powered sensors, wearable devices, and charging electronic devices [51]. Sound waves are mechanical waves. It will cause periodic changes in the surrounding air pressure during propagation. Thus, electric signals would be triggered when sound waves arrive at TENGs. For example, H. Zhao et al. proposed dual-tube helmholtz resonator-based TENG for highly efficient harvesting of acoustic energy [52]. G. M. Rani et al. reported CF-CNT based TENG for sound energy harvesting [53]. The output voltage is relatively low of below 5 V. Thus, sound sensitive TENGs are still needed to be optimized. In our case, SFS-TENG is proposed. To improve the sensitivities, a perforated acrylic sheet and copper mesh are adopted to allow the sound wave to pass through. Figures 3(a) and 3(b) show AFM surface morphologies of the PEEK film and the PTFE film, respectively. The surface Rms values are ~ 2.34 and ~ 6.35 nm, respectively. Figure 3(c) schematically shows the operation mechanisms for the present SFS-TENG. When the sound-wave amplitude reaches the valley, the PEEK film and the PTFE film come into full contact. Due to frictional electrification and electrostatic induction effects, the PTFE film will gain electrons, while the PEEK film will lose electrons. When the sound-wave amplitude increases, the PEEK film gradually moves away from the PTFE film and forms a potential difference between the two back electrodes (i.e., copper mesh), driving electrons from the bottom electrode to the top electrode. When the sound-wave amplitude reaches the peak, the PEEK film and PTFE film are sufficiently separated, and electrostatic equilibrium is reached between the two back electrodes. Now, there is no current in external circuit. As the sound-wave amplitude gradually decreases, the PEEK film approaches the PTFE film again. Thus, the potential difference between the two back electrodes gradually decreases, driving electrons to flow back from the top electrode to the bottom electrode. Therefore, when the sound loaded on SFS-TENGs undergoes periodic changes, an alternating voltage can be generated.

Figure 3(d) shows open circuit voltages (V_{OC}) of the SFS-TENG generated by sound wave signals with different frequencies at a fixed sound pressure level (SPL) of 100 dB. The V_{OC} value increases with the increased frequency from 20 to 350 Hz. Then, it decreases with the increased frequency from 350 to 20,000 Hz. The peak V_{OC} value is ~ 22.8 V. Thus, the present SFS-TENG has a resonant frequency of ~ 350 Hz. Figure S3(a) in the ESM shows V_{OC} of the SFS-TENG by sounds with different frequencies at different SPLs. The resonant frequency is still at ~ 350 Hz. The effects of spacer

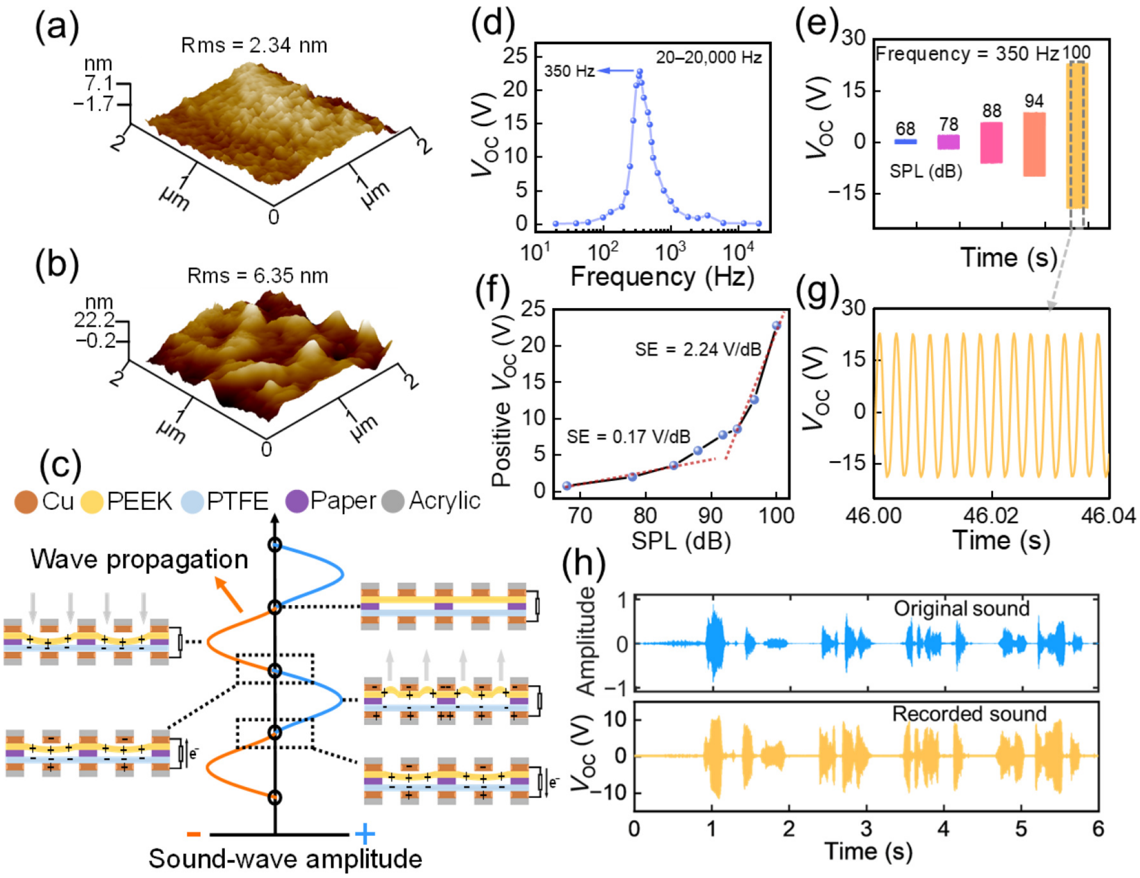

Figure 3 (a) AFM surface morphology of the PEEK film. (b) AFM surface morphology of the PTFE film. (c) Schematic diagram of the operating mechanism of the SFS-TENG. (d) V_{OC} of the S-TENG generated by sound wave signals with different frequencies at a fixed SPL of 100 dB. (e) V_{OC} characteristics of the SFS-TENG triggered by sound with different SPLs at the fixed sound frequency of 350 Hz. (f) Positive V_{OC} values as a function of SPL values at the fixed sound frequency of 350 Hz. (g) Enlarged image of V_{OC} responses generated by a sound (350 Hz, 100 dB). (h) Comparison of the waveform of a piece of sound with the recorded V_{OC} signals.

thicknesses on performances of SFS-TENG were also investigated, as shown in Fig. S3(b) in the ESM for sound signal (350 Hz, 100 dB). The V_{OC} responses of SFS-TENG decrease with the increased spacer thicknesses. Figure S3(c) in the ESM shows V_{OC} of the SFS-TENG by sounds with different frequencies at different spacer thicknesses. Again, the resonant frequency is still at ~ 350 Hz. Figure 3(e) shows V_{OC} characteristics of the SFS-TENG triggered by sound with different SPLs at the fixed sound frequency of 350 Hz. V_{OC} value gradually increases with the increased SPL value. The increased SPL enhances friction between the PEEK film and the PTFE film, resulting in the increased V_{OC}. Figure 3(f) shows the positive V_{OC} values as a function of SPL values. Here, the sensitivity is defined as: SE = $\Delta V_{OC}/\Delta$SPL. When the SPL value is below 84 dB, the SE value is estimated to be ~ 0.17 V/dB. When the SPL exceeds 90 dB, the SE value reaches ~ 2.24 V/dB. Table 1 compares typical parameters of the previously reported TENG based auditory perceptual systems. The sensitivities are ranged between 0.3 and 0.8 V/dB. While the present SFS-TENG demonstrates higher sensitivity. Interestingly, the present device processing is much simpler. Figure S4(a) in the ESM shows V_{OC} responses generated by a sound (350 Hz, 100 dB). Figure 3(g) shows the enlarged image of the V_{OC} response. It can be observed that the V_{OC} curve conforms to the propagation characteristics of sound wave. Figure S4(b) in the ESM shows rectified V_{OC} for a sound (350 Hz, 100 dB). Obviously, unipolar output is obtained after rectification, as is helpful for triggering neuromorphic responses in auditory perceptual systems. There is a slight decrease in V_{OC} from ~ 22.8 to ~ 15.6 V after rectification. Figure S4(c) in the ESM shows V_{OC} generated by the same sound after 85 days. The V_{OC} value decreases from ~ 22.8 to ~ 22.1 V. There is only slight decrease of ~ 3.1%. Figure S4(d) in the ESM shows V_{OC} generated by the same sound after 200 days. The measurements last for 2000 s. There are almost no changes in V_{OC}. The results demonstrate good durabilities of the SFS-TENG. Here, a speech sound was loaded on the SFS-TENG. Figure 3(h) compares the recorded V_{OC} signals with the waveform of the sound. The reproducibilities are quite well. We have also conducted tests on the dependences of output voltage (U), output current (I), and instantaneous power on external load resistances. The SFS-TENG is driven by a fixed sound signal (350 Hz,100 dB). Figures S4(e) and S4(f) in the ESM show the U, I, and power values under different external load resistances.

The previous results indicate that the SFS-TENG can effectively receive sound signals and convert them into electrical signals, while oxide neuromorphic transistors could receive and process these electrical signals in real time. Thus, an adaptive artificial auditory perceptual system (AAPS) can be proposed by integrating the SFS-TENG with the oxide neuromorphic transistor, as schematically shown in Fig. 1(b). Figure S5(a) in the ESM shows EPSC response of the AAPS on the loading of a sound (350 Hz, 100 dB) with duration of 5 s. The EPSC value rapidly increases during the loading of sound and gradually returns to the initial level after the

Table 1 Typical parameters of the previously reported TENG based auditory perceptual systems

Electrolyte layer	Channel	Friction layer	Electrode of TENG	Voltage	Sensitivity	Refs.
Ion-gel	PDVT-10	FEP film (processed by laser)	Au (vacuum sputtering)	~ 3.2 V at 110 dB 857 Hz	0.65 V/dB	[42]
Ta_2O_5	ITO	Needle punched FEP film	Cu (vacuum sputtering)	~ 3.1 V at 110 dB 1000 Hz	0.60 V/dB	[43]
SiO_2	IGZO	PTFE film	Conductivefabric	~ 23 V at 110 dB 180 Hz	0.77 V/dB	[46]
SiO_2	IGZO	FEP film	Conductivefabric	~ 6.4 V at 105 dB 180 Hz	0.36 V/dB	[47]
Chitosan	ITO	PEEK film	Cu mesh	~ 23 V at 100 dB 350Hz	2.24 V/dB	This work

sound ends. The peak EPSC value is ~ 28.1 μA. Here, the effects of SPLs on EPSC responses were investigated. Figure 4(a) shows peak EPSC values as a function of SPL values at fixed sound frequency of 350 Hz. It increases slowly when the SPL is below 95 dB. As the SPL exceeds 96 dB, the peak EPSC value increases rapidly. From a subjective perspective, the perception activities will be different for sound with gradually increased SPL values (case I) and for sound with gradually decreased SPL values (case II). Such behavior can also be mimicked on the present AAPS. Here, step-like sounds with either gradually increased SPL values from 68 to 100 dB (case I) or gradually decreased SPL values from 100 to 68 dB (case II) were loaded on the SFS-TENG. The duration time is 5 s. Figures 4(b) and 4(c) show the EPSC responses for case I and case II, respectively. For case I, the peak EPSC value is ~ 13.3 μA. While for case II, the peak EPSC value is only ~ 8.6 μA. As discussed above, the V_{OC} value of SFS-TENG will increase gradually for case I. While it will decrease gradually for case II. Thus, the peak EPSC value is obtained at the time when the sound ends for case I. While the peak EPSC value is obtained at the middle of the sound for case II. The behavior is consistent with those observed in Fig. 2(g).

Figure 4(d) shows EPSC responses on a noise (350 Hz, 30 s) at different SPLs. We set the noise tolerance threshold to 3 μA. When the EPSC current exceeds the threshold, it is assumed to be harmful to human auditory system. When the SPL is relatively low (≤ 92.4 dB), the EPSC value does not exceed the threshold. When the SPL reaches ~ 95.7 dB, the EPSC value exceeds the threshold after receiving noise for ~ 2.96 s. The peak EPSC value is ~ 3.7 μA, slightly higher than the threshold, indicating relatively safe condition. When the SPL reaches ~ 98.2 dB, the EPSC value exceeds the threshold after receiving noise for ~ 0.74 s. It rapidly increases to ~ 9 μA in a short time. The peak value is ~ 13.1 μA. The results indicate that the high SPL would potentially damage the human auditory system. Here, shouted sound was also loaded on the AAPS to trigger EPSC. Figure S5(b) in the ESM shows the waveform of a shouted sound of letter "A". Figure 4(e) shows corresponding EPSC responses triggered by shouted sounds of letter "A" with different SPLs. With the increased SPL values from ~ 90 to ~ 101.2 dB, the peak EPSC values increase from ~1.0 to ~15.9 μA. Figure 4(f) shows EPSC responses triggered by repeated shouted sounds of letter "A" under the constant SPL of ~ 96.3 dB. The peak EPSC value triggered by a single shouted sound of letter "A" is ~ 5.9 μA. It quickly returns to the initial current level when the shout ends. However, the peak EPSC value triggered by successive 25 shouted sounds of letter "A" reaches at ~ 27.9 μA. It remains at ~ 2.2 μA when the shouts end. The value is larger than the initial current level of ~ 0.5 μA. The results indicate the sensitivity of the present AAPS.

Additionally, frequency is also an important parameter of sounds. Thus, it is also interesting to study the effects of sound frequency on EPSC responses of the AAPS. In our case, the SPL value and the sound duration are fixed at 100 dB and 3 s, respectively. Figure 5(a) shows a typical EPSC response triggered by

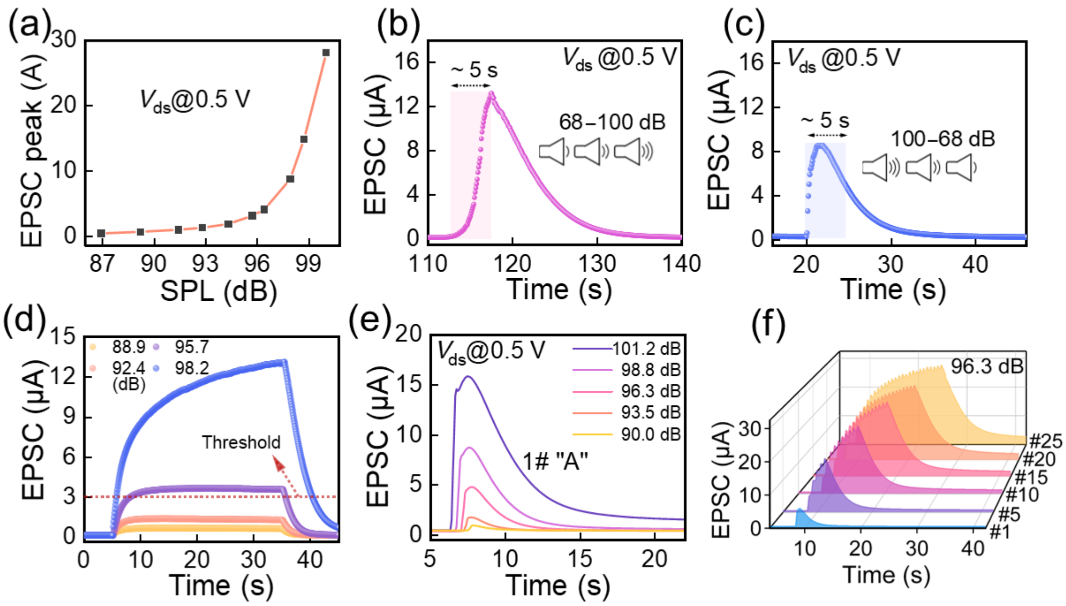

Figure 4 (a) Peak EPSC values of the AAPS as a function of SPL values at fixed sound frequency of 350 Hz. (b) EPSC response triggered by sound with increased SPL values from 68 to 100 dB (case I). (c) EPSC response triggered by sound with decreased SPL values from 100 to 68 dB (case I). (d) EPSC response triggered by a noise (350 Hz, 30 s) under different SPLs. (e) EPSC response triggered by a shouted sound of letter "A" with different SPLs. (f) EPSC response triggered by repeated shouted sounds of letter "A" under the constant SPL of 96.3 dB.

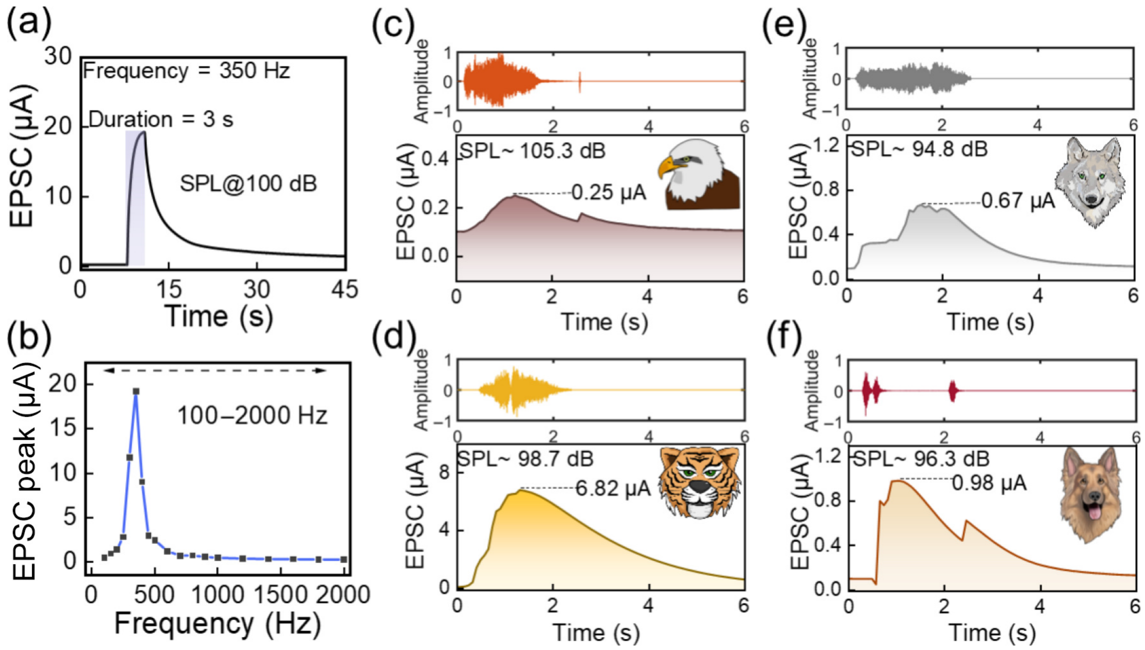

Figure 5 (a) EPSC response of AAPS triggered by a sound (350 Hz, 100 dB) with duration of 3 s. (b) EPSC peak values at different frequencies with fixed SPL and duration of 100 dB and 3 s, respectively. (c) EPSC response triggered by an eagle roar. (d) EPSC response triggered by a tiger roar. (e) EPSC response triggered by a wolf roar. (f) EPSC response triggered by a dog bark.

sound (350 Hz, 100 dB). The EPSC peak value is ~ 19.3 μA. Figure 5(b) shows the EPSC peak values at different frequencies. It increases with the increased frequency from 100 to 350 Hz. Then, it decreases with the increased frequency from 350 to 2000 Hz. It could be found that the most sensitive frequency is ranged between 250 and 450 Hz. As comparison, human being can easily recognize animals from their roars. Interestingly, the present AAPS can mimic such functions. Figures 5(c) and 5(d) show EPSC responses triggered by an eagle roar and a tiger roar, respectively. The time domain waveform of sound is also displayed at the upper panel of each figure. Though the SPL of eagle roar can reach ~ 105.3 dB, higher than that of tiger roar of ~ 98.7 dB, the EPSC peak value triggered by eagle roar is only ~ 0.25 μA, much lower than that of tiger roar of ~ 6.82 μA. Figures S6(a) and S6(b) in the ESM show frequency domain waveforms of eagle roar and tiger roar, respectively. For eagle roar, the spectrum locates mainly from ~ 1900 to ~ 2700 Hz with the peak at ~ 2248 Hz. While for tiger roar, the spectrum locates mainly from ~ 100 to ~ 500 Hz with the peak at ~ 269 Hz. Since the AAPS is sensitive for sound with frequency ranged between 250 and 450 Hz, the response on tiger roar will be much stronger than that on eagle roar. Figures 5(e) and 5(f) also show EPSC responses triggered by a wolf roar and a dog bark, respectively. The SPL values of wolf roar and dog bark are ~ 94.8 and ~ 96.3 dB, respectively. The EPSC peak value from wolf roar is ~ 0.67 μA, slightly lower than that of dog bark of ~ 0.98 μA. Figures S6(c) and S6(d) in the ESM show frequency domain waveforms of wolf roar and dog bark, respectively. It can be found that they have similar sound characteristics. Thus, it is quite normal for the similar EPSC responses on the two sounds.

Morse cipher is a renowned information coding method. It is capable of encoding letters, numbers, and certain punctuation marks using dots and dashes. The present AAPS also has potentials in information coding and decoding, as schematically shown in Fig. 6(a). When a series of sound signals are loaded on the SFS-TENG, the transistor will produce corresponding EPSC responses. The detected EPSC responses carry dot signal and dash signal and could be used for information decoding. Firstly, sounds with duration of 0.3 and 1 s are defined as "·" signal and "-" signal. The frequency and the SPL value are fixed at ~ 350 Hz and ~ 92.8 dB, respectively. Figure 6(b) shows the time domain waveform of sound trains with different duration times. The time interval between each sound signal is 1 s, while the time interval between each group of signals is 2 s. Figure 6(c) shows EPSC response triggered by the sound trains in Fig. 6(b). Here, a threshold EPSC value of 0.4 μA is set. For EPSC value that exceeds the threshold, a dash signal can be decoded. Otherwise, a dot signal can be decoded. Thus, Figure 6(c) can be decoded as "-·", "·", "··-", "·-·", "---", and "-·", corresponding to a word "NEURON". Interestingly, the present AAPS would have different responses on sounds with different frequencies, though the sound has similar SPL. Thus, another information encryption and decryption strategy can also be proposed. Sounds with frequencies of 450 and 350 Hz are treated as "·" signal and "-" signal, respectively. The SPL values and the duration time are fixed at 92.8 dB and 1 s, respectively. Figure 6(d) shows the time domain waveform of sound trains with different frequencies. The sound trains are less likely to be distinguishable by our ear. Figure 6(e) shows the EPSC response triggered by the sound trains in Fig. 6(d). Corresponding video materials are also provided in the ESM. Interestingly, EPSC with different levels can be observed. It can be decoded as "···", "-·--", "-·", "·-", "·--·", "···", and "·", corresponding to a word "SYNAPSE". Here, sounds with same durations of 1 s can still be decrypted as "·" or "-" signal based on frequencies. Thus, the encryption strategy based on frequency is superior than that based on sound duration.

It is well known that Doppler effect is a phenomenon that occurs when there is a relative motion between a wave source and an observer. The frequency will increase/decrease when the source is approaching to/departing from an observer [48, 49, 54]. It is crucial in science and technology, allowing us to understand motion and behavior of waves in different contexts. In terms of high-speed

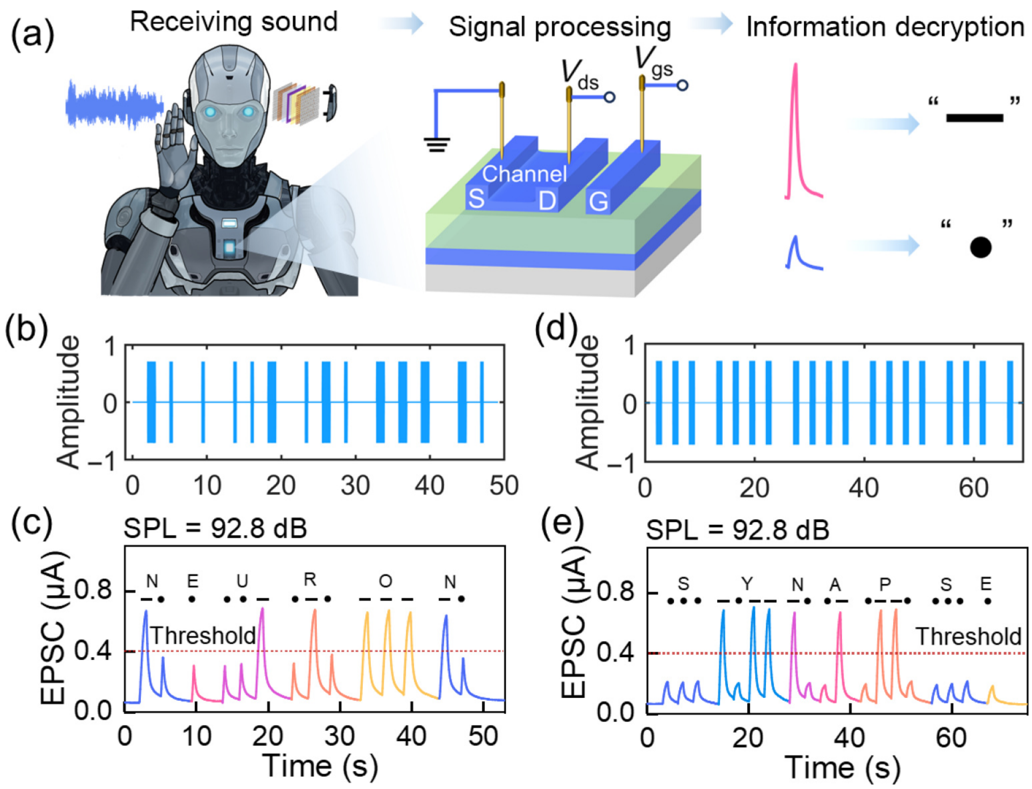

Figure 6 (a) Schematic illustration of information encryption and decryption process based on AAPS. (b) Time domain waveform of sound trains with different duration times, i.e., 0.3 and 1 s, carrying information of "NEURON". (c) EPSC response triggered by the sound trains in (b). The EPSC response can be decoded to obtain a word "NEURON". (d) Time domain waveform of sound trains with different frequencies, i.e., 450 and 350 Hz, carrying information of "SYNAPSE". (e) EPSC response triggered by the sound trains in (d). The EPSC response can be decoded to obtain a word "SYNAPSE".

driving, cars will inevitably encounter emergencies that require drivers to brake urgently to avoid danger. Therefore, the performance of car brake is one of the key factors affecting safe driving. Considering the fact that the present AAPS has frequency dependent responses, a brake performance testing scheme can be proposed based on the present AAPS and Doppler effect, as schematically shown in Fig. 7(a). When a sound source approaches an observer, the frequency can be described as follows

$$F = [V_0/(V_0 - V)] \cdot F_0 \tag{2}$$

where F, F_0, V, and V_0 are the frequency perceived by the observer, the frequency of the sound source, the velocity of the sound source relative to ground, and the speed of sound wave propagation in air, respectively. If the sound source emits sound with frequency of 300 Hz, the frequency perceived by the observer will increase if the sound source approaches the observer, as shown in Fig. 7(b). When the car equipped with a sound source (300 Hz, 100 dB) passes through the detector at different speeds, sound signals with different frequencies at similar SPL value of 100 dB will be loaded on SFS-TENG equipped in the detector, generating different V_{OC} values. As shown in Fig. 7(c), V_{OC} values of SFS-TENG increase with the increased car speeds. At speeds of 100 and 20 km/h, the V_{OC} values are ~ 21.4 and ~ 19.7 V, respectively. Figure 7(d) schematically shows internal structure and signal processing unit of the detector. The V_n terminal of the voltage comparator is set at certain values to assure the effective assessment of brake performances. For the first velocity detector, the V_n is set at 21.4 V. For the second velocity detector, the V_n is set at 19.7 V. The V_p terminal receives the electrical signals produced by the SFS-TENG. The voltage comparator will output a high-level signal when $V_p > V_n$ and a low-level signal when $V_p < V_n$. When the car passes through first detector at a speed over 100 km/h, the V_{OC} of SFS-TENG instantly exceeds 21.4 V. Thus, the comparator triggers a high-level spike signal of 2 V. The spike will be loaded on the gate to trigger a small EPSC response. After braking for a distance of 60 m, the car will pass through the second detector. If the speed is still above 20 km/h, the V_{OC} of SFS-TENG will exceed 19.7 V. Thus, another spike signal of 4 V will be triggered, which will trigger a larger EPSC response. As shown in Fig. 7(e), if only one smaller EPSC peak is detected, the braking performance is considered to be qualified. In another word, the car at a speed over 100 km/h can reduce the speed to a safe level (< 20 km/h) within a braking distance of 60 m. The above results indicate that the present AAPS has certain prospects, including intelligent sound positioning, bionic intelligent auditory system, and prosthetic artificial ear, etc.

4 Conclusions

In summary, an artificial auditory perceptual system is proposed by integrating SFS-TENGs with ITO ionotronic neuromorphic transistors. The SFS-TENG can convert sound wave signals into electrical signals, exhibiting a high sensitivity of ~ 2.24 V/dB and good durability. The ITO ionotronic neuromorphic transistor can further process the electrical signals generated by the SFS-TENG. Thus, the system can simulate the auditory perception of the brain, exhibiting a wide range of sound pressure and frequency recognition capabilities. Thus, information encryption/decryption

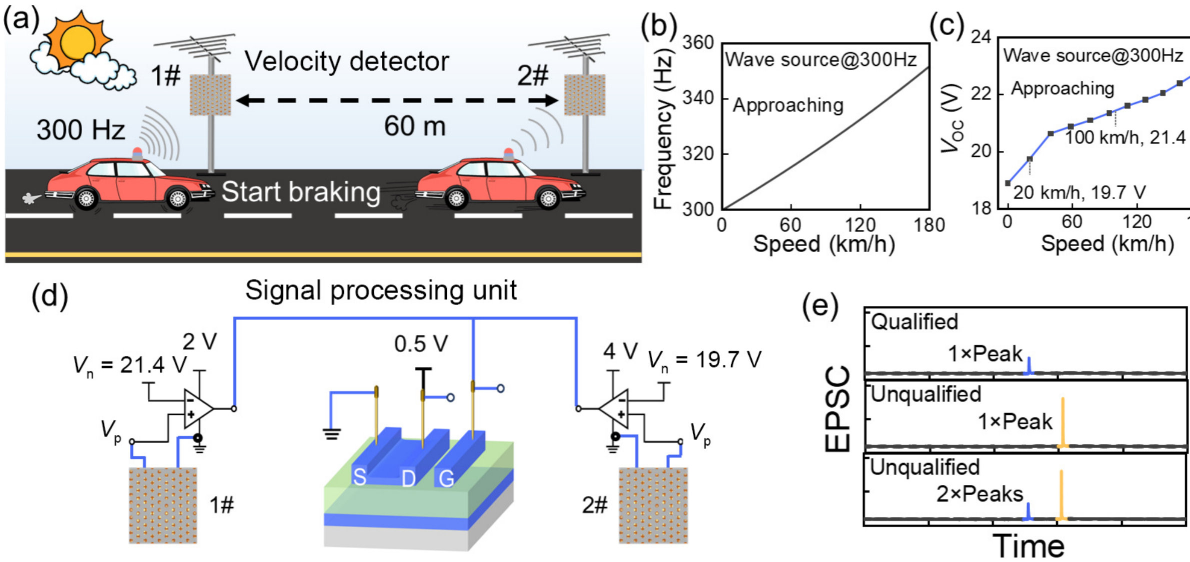

Figure 7 (a) Schematic diagram of the brake performance testing scheme with Doppler effect based on the present AAPS. (b) Frequency perceived by the observer as a function of approaching sound source speed. The frequency of the sound source is 300 Hz. (c) V_{OC} of SFS-TENG as a function of car speed. (d) Schematic diagram of internal structure and signal processing unit of the detector. (e) Test results of car braking performances.

and Doppler frequency shift temporal information processing are demonstrated. The present auditory perceptual system demonstrates broad application prospects, providing new opportunities to create sophisticated, adaptable, and interactive systems.

Electronic Supplementary Material: Supplementary material (flow chart of the fabrication processing of ITO neuromorphic transistors, physical image of testing figuration, leakage current of chitosan film, EPSC responses, V_{OC} of the SFS-TENG, output voltage/current and output power of SFS-TENG on different external load resistances, EPSC value under sound, frequency domain waveforms of sound, and video materials of real-time information decryption) is available in the online version of this article at https://doi.org/10.26599/NR.2025.94907378.

Data availability

All data needed to support the conclusions in the paper are presented in the manuscript and the Electronic Supplementary Material.

Acknowledgements

This work is granted by the National Natural Science Foundation of China (No. U22A2075) and Ningbo Key Scientific and Technological Project (No. 2021Z116).

Declaration of competing interest

All the contributing authors report no conflict of interests in this work.

Author contribution statement

S. Y. Z.: Data curation, methodology, validation, experimental design, writing – original draft. W. S. W.: Data curation, methodology, validation. X. H.: Data curation. B. C. G.: Validation. J. K. D.: Methodology. Y. J. H.: Validation. L. Q. Z.: Methodology, project administration, funding acquisition, writing – review & editing. All the authors have approved the final manuscript.

Use of AI statement

None.

References

[1] LeCun, Y.; Bengio, Y.; Hinton, G. Deep learning. *Nature* **2015**, *521*, 436–444.

[2] Mariantoni, M.; Wang, H.; Yamamoto, T.; Neeley, M.; Bialczak, R. C.; Chen, Y.; Lenander, M.; Lucero, E.; O'Connell, A. D.; Sank, D. et al. Implementing the quantum von Neumann architecture with superconducting circuits. *Science* **2011**, *334*, 61–65.

[3] Musib, M.; Wang, F.; Tarselli, M. A.; Yoho, R.; Yu, K. H.; Andrés, R. M.; Greenwald, N. F.; Pan, X. B.; Lee, C. H.; Zhang, J. et al. Artificial intelligence in research. *Science* **2017**, *357*, 28–30.

[4] Li, C.; Zhang, X.; Li, J. W.; Fang, T.; Dong, X. W. The challenges of modern computing and new opportunities for optics. *PhotoniX* **2021**, *2*, 20.

[5] Mead, C. Neuromorphic electronic systems. *Proc. IEEE* **1990**, *78*, 1629–1636.

[6] Furber, S. To build a brain. *IEEE Spectrum* **2012**, *49*, 44–49.

[7] Machens, C. K. Building the human brain. *Science* **2012**, *338*, 1156–1157.

[8] Lu, Y.; Alvarez, A.; Kao, C. H.; Bow, J. S.; Chen, S. Y.; Chen, I. W. An electronic silicon-based memristor with a high switching uniformity. *Nat. Electron.* **2019**, *2*, 66–74.

[9] Xiong, W.; Zhu, L. Q.; Ye, C.; Ren, Z. Y.; Yu, F.; Xiao, H.; Xu, Z.; Zhou, Y.; Zhou, H.; Lu, H. L. Flexible poly(vinyl alcohol)-graphene oxide hybrid nanocomposite based cognitive memristor with pavlovian-conditioned reflex activities. *Adv. Electron. Mater.* **2020**, *6*, 1901402.

[10] Hu, L. X.; Yang, J.; Wang, J. R.; Cheng, P. H.; Chua, L. O.; Zhuge, F. All-optically controlled memristor for optoelectronic neuromorphic computing. *Adv. Funct. Mater.* **2021**, *31*, 2005582.

[11] Zhao, X. N.; Xu, J. Q.; Xie, D.; Wang, Z. Q.; Xu, H. Y.; Lin, Y.; Hu, J. L.; Liu, Y. C. Natural acidic polysaccharide-based memristors for

transient electronics: Highly controllable quantized conductance for integrated memory and nonvolatile logic applications. *Adv. Mater.* **2021**, *33*, 2104023.
[12] Shim, H.; Ershad, F.; Patel, S.; Zhang, Y. C.; Wang, B. H.; Chen, Z. H.; Marks, T. J.; Facchetti, A.; Yu, C. J. An elastic and reconfigurable synaptic transistor based on a stretchable bilayer semiconductor. *Nat. Electron.* **2022**, *5*, 660–671.
[13] Merces, L.; Ferro, L. M. M.; Nawaz, A.; Sonar, P. Advanced neuromorphic applications enabled by synaptic ion-gating vertical transistors. *Adv. Sci.* **2024**, *11*, 2470162.
[14] Wang, W. S.; Shi, Z. W.; Chen, X. L.; Li, Y.; Xiao, H.; Zeng, Y. H.; Pi, X. D.; Zhu, L. Q. Biodegradable oxide neuromorphic transistors for neuromorphic computing and anxiety disorder emulation. *ACS Appl. Mater. Interfaces* **2023**, *15*, 47640–47648.
[15] Wang, C. Y.; Bian, Y. S.; Liu, K.; Qin, M. C.; Zhang, F.; Zhu, M. L.; Shi, W. K.; Shao, M. C.; Shang, S. C.; Hong, J. X. et al. Strain-insensitive viscoelastic perovskite film for intrinsically stretchable neuromorphic vision-adaptive transistors. *Nat. Commun* **2024**, *15*, 3123.
[16] Wang, J. X.; Lin, M. F.; Park, S.; Lee, P. S. Deformable conductors for human-machine interface. *Mater. Today* **2018**, *21*, 508–526.
[17] Lin, Z. W.; Zhang, G. Q.; Xiao, X.; Au, C.; Zhou, Y. H.; Sun, C. C.; Zhou, Z. H.; Yan, R.; Fan, E. D.; Si, S. B. et al. A personalized acoustic interface for wearable human–machine interaction. *Adv. Funct. Mater.* **2022**, *32*, 2109430.
[18] Wei, Y.; He, Y. Y.; Wang, C. Y.; Chen, G.; Zhao, B. X. Asymmetric "Janus" biogel for human–machine interfaces. *Adv. Funct. Mater.* **2023**, *33*, 2214366.
[19] Haick, H.; Tang, N. Artificial intelligence in medical sensors for clinical decisions. *ACS Nano.* **2021**, *15*, 3557–3567.
[20] Zhao, P. F.; Song, Y. L.; Hu, Z. P.; Zhong, Z. H.; Li, Y.; Zhou, K.; Qin, T. T.; Yan, Y.; Hsu, H. H.; Han, S. T. et al. Artificial intelligence enabled biodegradable all-textile sensor for smart monitoring and recognition. *Nano Energy* **2024**, *130*, 110118.
[21] Feng, H.; Lv, Y. S.; Yang, X.; Wang, J.; Zhang, X. X.; Pei, X. B. Bimodal visual sensors based on mechanoluminescence and biosensing for artificial intelligence-assisted orthodontics, *Adv. Funct. Mater.* **2025**, *35*, 2416437.
[22] Hou, X. Y.; Xin, L. B.; Fu, Y. L.; Na, Z.; Gao, G. W.; Liu, Y. H.; Xu, Q. Z.; Zhao, P. T.; Yan, G. Z.; Su, Y. L. et al. A self-powered biomimetic mouse whisker sensor (BMWS) aiming at terrestrial and space objects perception. *Nano Energy* **2023**, *118*, 109034.
[23] Lin, W. E.; Wang, Z. Y.; Xu, Y. T.; Hu, Z. X.; Zhao, W. Y.; Zhu, Z. H.; Sun, Z. L.; Wang, G. X.; Peng, Z. C. Self-adaptive perception of object's deformability with multiple deformation attributes utilizing biomimetic mechanoreceptors. *Adv. Mater* **2024**, *36*, 2305032.
[24] Chen, C. Z.; Liu, Z. J.; Guo, L. C.; Huo, B. C.; Sun, Q.; Liang, L. R.; Du, C. Y.; Chen, G. M. High spatiotemporal resolution biomimetic thermoreceptors realizing by jointless p-n integration thermoelectric composites. *Adv. Funct. Mater.* **2024**, *34*, 2411490.
[25] Ouyang, H.; Li, Z.; Gu, M.; Hu, Y. R.; Xu, L. L.; Jiang, D. J.; Cheng, S. J.; Zou, Y.; Deng, Y.; Shi, B. J. et al. A bioresorbable dynamic pressure sensor for cardiovascular postoperative care. *Adv. Mater.* **2021**, *33*, 2102302.
[26] Park, Y. J.; Ro, Y. G.; Shin, Y. E.; Park, C.; Na, S.; Chang, Y.; Ko, H. Multi-layered triboelectric nanogenerators with controllable multiple spikes for low-power artificial synaptic devices. *Adv. Sci.* **2023**, *10*, 2304598.
[27] Lei, H.; Yin, Z. Y.; Huang, P. H.; Gao, X.; Zhao, C.; Wen, Z.; Sun, X. H.; Wang, S. D. Intelligent tribotronic transistors toward tactile near-sensor computing. *Adv. Funct. Mater.*, in press, https://doi.org/10.1002/adfm.202401913.
[28] Han, C.; Han, X. W.; Han, J. Y.; He, M. Y.; Peng, S. L.; Zhang, C. Y.; Liu, X. C.; Gou, J.; Wang, J. Light-stimulated synaptic transistor with high PPF feature for artificial visual perception system application. *Adv. Funct. Mater* **2022**, *32*, 2113053.
[29] Cheng, Y. K.; Li, Z.; Lin, Y.; Wang, Z. Q.; Shan, X. Y.; Tao, Y.; Zhao, X. N.; Xu, H. Y.; Liu, Y. C. Color recognition achieved in multiwavelength controlled plasmonic optoelectronic memristor for neuromorphic visual system. *Adv. Funct. Mater.* **2025**, *35*, 2414404.
[30] Wan, H. C.; Zhao, J. Y.; Lo, L. W.; Cao, Y. Q.; Sepúlveda, N.; Wang, C. Multimodal artificial neurological sensory-memory system based on flexible carbon nanotube synaptic transistor. *ACS Nano.* **2021**, *15*, 14587–14597.
[31] Shinn-Cunningham, B. G. Object-based auditory and visual attention. *Trends Cogn. Sci.* **2008**, *12*, 182–186.
[32] Jasmin, K.; Lima, C. F.; Scott, S. K. Understanding rostral-caudal auditory cortex contributions to auditory perception. *Nat. Rev. Neurosci.* **2019**, *20*, 425–434.
[33] Ahmadi, H.; Moradi, H.; Pastras, C. J.; Abolpour Moshizi, S.; Wu, S. Y.; Asadnia, M. Development of ultrasensitive biomimetic auditory hair cells based on piezoresistive hydrogel nanocomposites. *ACS Appl. Mater. Interfaces* **2021**, *13*, 44904–44915.
[34] Jung, Y. H.; An, J.; Hyeon, D. Y.; Wang, H. S.; Kim, I.; Jeong, C. K.; Park, K. I.; Lee, P. S.; Lee, K. J. Theoretical basis of biomimetic flexible piezoelectric acoustic sensors for future customized auditory systems. *Adv. Funct. Mater.* **2024**, *34*, 2309316.
[35] Zhu, K.; Yan, B. Biomimetic Eu@HOF photoactivated sponge as ultrasensitive auditory and olfactory sensor for infrasound wave monitoring and bimodal information integration. *Adv. Funct. Mater.* **2024**, *34*, 2401395.
[36] Fan, F. R.; Tian, Z. Q.; Wang, Z. L. Flexible triboelectric generator. *Nano Energy.* **2012**, *1*, 328–334.
[37] Chen, F. Q.; Wu, Y. H.; Ding, Z. Y.; Xia, X.; Li, S. H.; Zheng, H. W.; Diao, C. L.; Yue, G. T.; Zi, Y. L. A novel triboelectric nanogenerator based on electrospun polyvinylidene fluoride nanofibers for effective acoustic energy harvesting and self-powered multifunctional sensing. *Nano Energy,* **2019**, *56*, 241–251.
[38] Liu, X. R.; Zhao, Z. H.; Gao, Y. K.; Nan, Y.; Hu, Y. X.; Guo, Z. T.; Qiao, W. Y.; Wang, J.; Zhou, L. L.; Wang, Z. L. et al. Triboelectric nanogenerators exhibiting ultrahigh charge density and energy density. *Energy Environ. Sci.* **2024**, *17*, 3819–3831.
[39] Ouyang, H.; Li, Z. The first technology can compete with piezoelectricity to harvest ultrasound energy for powering medical implants. *Sci. Bull.* **2019**, *64*, 1565–1566.
[40] Yao, H. B.; Wang, Z. X.; Wu, Y. H.; Zhang, Y. Z.; Miao, K. X.; Cui, M.; Ao, T. Y.; Zhang, J. W.; Ban, D. Y.; Zheng, H. W. Intelligent sound monitoring and identification system combining triboelectric nanogenerator-based self-powered sensor with deep learning technique. *Adv. Funct. Mater.* **2022**, *32*, 2112155.
[41] Guo, H. Y.; Pu, X. J.; Chen, J.; Meng, Y.; Yeh, M. H.; Liu, G. L.; Tang, Q.; Chen, B. D.; Liu, D.; Qi, S. et al. A highly sensitive, self-powered triboelectric auditory sensor for social robotics and hearing aids. *Sci. Robot* **2018**, *3*, eaat2516.
[42] Liu, Y. Q.; Li, E. L.; Wang, X. M.; Chen, Q. Z.; Zhou, Y. L.; Hu, Y. Y.; Chen, G. X.; Chen, H. P.; Guo, T. L. Self-powered artificial auditory pathway for intelligent neuromorphic computing and sound detection. *Nano Energy* **2020**, *78*, 105403.
[43] Lian, Q. M.; Liu, Y. Q.; Zhang, X. H.; Shan, L. T.; Wu, X. M.; Chen, H. P.; Guo, T. L. Noise detection system based on noise triboelectric nanogenerator and synaptic transistors. *IEEE Electron Device Lett.* **2021**, *42*, 1334–1337.
[44] Wu, X. M.; Li, E. L.; Liu, Y. Q.; Lin, W. K.; Yu, R. J.; Chen, G. X.; Hu, Y. Y.; Chen, H. P.; Guo, T. L. Artificial multisensory integration

nervous system with haptic and iconic perception behaviors. *Nano Energy* **2021**, *85*, 106000.

[45] Wei, Y. C.; Yu, J. R.; Li, Y. H.; Wang, Y. F.; Huo, Z. W.; Cheng, L. Q.; Yue, D. W.; Zhang, K. T.; Gong, J.; Wang, J. et al. Mechano-driven logic-in-memory with neuromorphic triboelectric charge-trapping transistor. *Nano Energy* **2024**, *126*, 109622.

[46] Ke, S.; Wang, F. Y.; Fu, C. Y.; Mao, H. W.; Zhu, Y. X.; Wang, X. J.; Wan, C. J.; Wan, Q. Artificial fear neural circuit based on noise triboelectric nanogenerator and photoelectronic neuromorphic transistor. *Appl. Phys. Lett.* **2023**, *123*, 123501.

[47] Wang, F. Y.; Ke, S.; Li, J. A.; Zhang, J. H.; Cheng, Y.; Huang, J. R.; Shi, Y.; Pan, L. J. Adaptively responsive self-powered bionic auditory device for sleep health monitoring. *IEEE Electron Device Lett.* **2023**, *44*, 1348–1351.

[48] Haubrich, W. S. Doppler of the Doppler ultrasound effect. *Gastroenterology* **2003**, *125*, 1590.

[49] Seddon, N.; Bearpark, T. Observation of the inverse Doppler effect. *Science* **2003**, *302*, 1537–1540.

[50] Chen, X. L.; Huang, X.; Li, Y.; Wang, W. S.; Huang, Y. J.; Xiao, H.; Wan, Q.; Zhu, L. Q. Triboelectric potential tuned oxide artificial tactile sensory platform with ultra-low power consumption. *Appl. Mater. Today* **2024**, *36*, 102034.

[51] Qiu, W. Z.; Feng, Y. G.; Luo, N.; Chen, S. G.; Wang, D. A. Sandwich-like sound-driven triboelectric nanogenerator for energy harvesting and electrochromic based on Cu foam. *Nano Energy* **2020**, *70*, 104543.

[52] Zhao, H. F.; Xiao, X.; Xu, P.; Zhao, T. C.; Song, L. G.; Pan, X. X.; Mi, J. C.; Xu, M. Y.; Wang, Z. L. Dual-tube helmholtz resonator-based triboelectric nanogenerator for highly efficient harvesting of acoustic energy. *Adv. Energy Mater.* **2019**, *9*, 1902824.

[53] Rani, G. M.; Wu, C. M.; Motora, K. G.; Umapathi, R.; Jose, C. R. M. Acoustic-electric conversion and triboelectric properties of nature-driven CF–CNT based triboelectric nanogenerator for mechanical and sound energy harvesting. *Nano Energy* **2023**, *108*, 108211.

[54] Zeng, T.; Wang, Z. Q.; Lin, Y.; Cheng, Y. K.; Shan, X. Y.; Tao, Y.; Zhao, X. N.; Xu, H. Y.; Liu, Y. C. Doppler frequency-shift information processing in WO_x-based memristive synapse for auditory motion perception. *Adv. Sci.* **2023**, *10*, 2300030.